Earth Planet. Sci. Lett. 690 (2026) 120163

Contents lists available at ScienceDirect

Earth and Planetary Science Letters

journal homepage: www.elsevier.com/locate/epsl

Fractures regulate coupled dissolution-precipitation dynamics: Regime map, optimal fracture conductance, and clogging

Agnieszka Budek [a], Piotr Szymczak [b], Peter K. Kang [a,c,*]

[a] Department of Earth and Environmental Sciences, University of Minnesota - Twin Cities, Minneapolis, Minnesota, USA
[b] Institute of Theoretical Physics, Faculty of Physics, University of Warsaw, Poland
[c] Saint Anthony Falls Laboratory, University of Minnesota Minneapolis, MN, 55414, USA

ARTICLE INFO

Editor: DR J BADRO

Keywords:
Dissolution-precipitation
Fractured porous media
Instability
Clogging
Pore network modeling

ABSTRACT

The interplay between dissolution and precipitation reactions critically governs the long-term evolution of geologic media, yet the role of fractures in shaping these dynamics remains poorly understood. Here we employ a pore-network modeling framework that explicitly represents both matrix pores and a through-going fracture to investigate coupled dissolution-precipitation processes. We show that fractures fundamentally alter system behavior, for example, by promoting extensive precipitation through side-branching instabilities. A comprehensive parametric study reveals three distinct regimes–passivation, side branching, and uniform replacement–emerging as functions of the Damköhler number and the Fogler number. Importantly, we identify an optimal fracture-to-matrix conductance ratio that maximizes secondary mineral deposition, whereas either absent or overly dominant fractures suppress precipitation. We also demonstrate that fractures can mitigate system clogging by redistributing precipitation away from the primary flow path into side branches. Under both constant flow and constant pressure inlet conditions, fractures reduce the likelihood of clogging by altering flow and reactive pathways. These results underscore the pivotal role of fractures in governing feedbacks among flow, transport, and reactions, with direct implications for geological processes such as diagenesis, ore formation, and carbon mineralization.

1. Introduction

Dissolution and precipitation within fractured porous rocks govern many of Earth's fundamental alteration processes. In sedimentary basins, basinal brines dissolve framework grains while promoting the precipitation of cement phases, thereby modulating reservoir quality through compactional cementation, silicification, and dolomitization (Korzhinskii, 1968; Fowler and Yang, 2003; Putnis and Mezger, 2004; Merino and Canals, 2011; Ulrich et al., 2014; Montes-Hernandez et al., 2016; Beinlich et al., 2020; Centrella et al., 2021). In volcanic and metamorphic terrains, hydrothermal replacement builds ore bodies (skarns, epithermal veins) as dissolving host minerals feed precipitating products along fracture-matrix networks (Putnis and Austrheim, 2012; Guo et al., 2021). In engineered settings, carbon mineralization, geothermal scaling, acidizing or in-situ leaching similarly depend on whether fractures deliver reactants deep into the rock matrix or shut down by filling with precipitate (Rege and Fogler, 1989; Eriksson and Destouni, 1997; Garcia-Rios et al., 2015; Pandey et al., 2015; Matter et al., 2016; Nitschke, 2018; Nisbet et al., 2024; Soucey et al., 2025; Shen et al., 2025). Across these systems, dissolution and precipitation proceed concurrently, coupled with evolving permeability and heterogeneous flow (Ruiz-Agudo et al., 2014; Kondratiuk et al., 2015; Putnis, 2021).

Coupled dissolution and precipitation exert a strong influence on subsurface flow properties. Dissolution can enhance permeability by widening pores and generating flow channels (Noiriel et al., 2013; Menke et al., 2015; Deng et al., 2015; Starchenko et al., 2016; Molins et al., 2021; Zhou et al., 2022; Deng et al., 2025; Lee et al., 2025), whereas precipitation often reduces permeability by clogging pore throats and conduits (Zhang et al., 2010; Noiriel et al., 2016; Jones and Detwiler, 2016; Poonoosamy et al., 2020; Nooraiepour et al., 2021; Yang et al., 2024b; Shafabakhsh et al., 2024; Yang et al., 2024a). The competition between these two processes could lead to diverse outcomes, ranging from permeability enhancement through wormholing to severe flow reduction due to passivation and clogging. Understanding when and how these feedbacks occur is essential for predicting the evolution of reactive transport systems in both natural and engineered settings.

Classical results cover end-members – wormholing in dissolution-only flows and passivation in precipitation-only systems – but field observations show mixed textures: lateral replacement bands off major fractures, arrested tips, alternations of sealed and open segments, and sharp contrasts in replacement depth across seemingly similar fracture

* Corresponding author.
E-mail address: pkkang@umn.edu (P.K. Kang).

https://doi.org/10.1016/j.epsl.2026.120163
Received 14 November 2025; Received in revised form 12 May 2026; Accepted 2 June 2026

sets (Palmer, 1991; Ford and Williams, 2007). Fractures play a pivotal role in this context. They are ubiquitous in rocks, frequently dominate subsurface flow, and provide preferential pathways for both fluids and chemical species. By focusing transport, fractures have the potential to strongly mediate dissolution-precipitation dynamics, redistributing reactions into the surrounding matrix and altering the balance between permeability enhancement and clogging.

Despite the recognized importance of fractures in reactive transport, previous studies have largely focused on dissolution and precipitation processes within individual fractures and on the evolution of preferential flow paths in fracture-dominated systems (Békri et al., 1997; Dijk et al., 2002; Wang et al., 2022; Kaufmann et al., 2016), while the role of coupled fracture-matrix interactions in governing multiscale reactive transport and mineral alteration remains less well understood.

In this study, we employ a pore-network modeling framework that explicitly represents both the porous matrix and a through-going fracture. The model ties chemistry (precipitation and dissolution reaction rates and mineral molar volumes) and hydraulic architecture (fracture-matrix contrast), and is capable of reproducing these observable patterns. Specific objectives are threefold: (1) to determine how fractures influence the competition between dissolution and precipitation and the resulting flow and transformation patterns; (2) to identify the conditions and mechanisms under which fractures promote passivation, side branching, or uniform mineral replacement; and (3) to quantify the extent to which fractures mitigate or exacerbate clogging under different flow boundary conditions.

2. Model

2.1. System description

In this work, we consider a system consisting of a single fracture embedded in a porous medium composed of a dissolving mineral A. Water containing reactive species is injected pointwise at the fracture inlet. The fracture is aligned with the pressure gradient and, at least initially, constitutes the main flow pathway. The reactants injected with the water drive both the dissolution of mineral A and the precipitation of mineral E within the system, with the two reactions being coupled.

To study reactive coupling, we consider a two-step process: (1) dissolution of mineral A by B ions, which releases coupling ions C into solution:

$$\text{Reaction 1:} \quad \chi_A \mathrm{A} + \chi_B \mathrm{B} \rightarrow \mathrm{C}^{\uparrow} \tag{1}$$

and (2) reaction of C with another ionic species D, forming the secondary mineral E:

$$\text{Reaction 2:} \quad \mathrm{C} + \chi_D \mathrm{D} \rightarrow \chi_E \mathrm{E}_{\downarrow}, \tag{2}$$

where χ_i denote the stoichiometric coefficients. Reaction is coupled via the coupling ion C that leads to the precipitation of mineral E. At the inlet, water containing B is injected, while the source of C is reaction (1), such that $c_B^{\mathrm{in}} > 0$ and $c_C^{\mathrm{in}} = 0$. Real-world examples of such coupled reactions include sandstone acidizing and mineral carbonation (Matter and Kelemen, 2009; Oelkers et al., 2008; Andreani et al., 2009; Sanna et al., 2014; Lund and Fogler, 1976; Economides and Nolte, 2000).

The transport and reaction of chemical species are governed by a convection-reaction equation integrated along individual pores,

$$\frac{\partial (q c_k)}{\partial x} = -\pi d R_k(c_1, \ldots, c_N). \tag{3}$$

We consider first-order, irreversible kinetics (Fredd and Fogler, 1998; Dreybrodt, 1990),

$$R_{\mathrm{diss}} = k_1 c_B, \qquad R_{\mathrm{prec}} = k_2 c_C, \tag{4}$$

where k_1 and k_2 represent the effective dissolution and precipitation rate constants, respectively, as in Budek and Szymczak (2025). Reactant D is assumed to be in excess, so the precipitation rate depends solely on the concentration of species C. Both reactions are therefore treated as single-species processes.

2.2. Numerical model details

To study the complex interplay between fluid flow, transport, and chemical reactions in porous media, we employ a pore-network modeling approach, following our previous methodology (Budek and Szymczak, 2012, 2025) which was an extension of the network model proposed by Hoefner and Fogler (1988), Rege and Fogler (1989). This framework offers a geometrically explicit and computationally efficient representation of porous rocks, allowing precise control over pore structure and resolution of concentration gradients at the pore scale. For this study, we extended our previous pore-network model to incorporate a through-going fracture intersecting the porous rock matrix, which acts as a preferential flow pathway.

Unlike traditional pore-network models, our approach tracks not only pore diameters but also the surrounding grain volumes. Their composition evolves over time, which determines the availability of dissolving material. In the network model (see Fig. 1a-b), we distinguish between pores where reactions occur (graph edges), pore intersections (graph nodes) where complete mixing of reactants is assumed, and grains (graph faces) representing the solid material undergoing dissolution or precipitation. Each node i is characterized by its pressure, $p_i(t)$, and the concentrations of reactants, $c_i^{B/C}(t)$. A pore ij, spanning nodes i and j, carries information about its geometry – diameter $d_{ij}(t)$ and length $l_{ij}(t)$ – as well as its volumetric flow rate, $q_{ij}(t)$. Finally, each grain ijk, defined by the triplet of nodes i, j, and k, is characterized by the volumes of solid materials A and E, $V_{ijk}^A(t)$ and $V_{ijk}^E(t)$. Note that dissolution reaction occurs only when $V_{ijk}^A(t) > 0$, and pore and grain geometries evolve over time as chemical reactions proceed within the system.

In this study, we employ a random triangular network composed of $N_x \times N_y$ nodes distributed within a rectangular domain of aspect ratio N_x/N_y. The (x, y) positions of the nodes are assigned randomly and independently of one another. The edges are constructed using Delaunay triangulation.

The pore structure used here should be interpreted as an idealized pore-network representation rather than as a direct reconstruction of a specific natural rock sample. The random Delaunay network captures a connected, disordered matrix pore space, whereas the imposed high-conductance pathway represents a through-going fracture. The model is therefore most directly relevant to fractured porous rocks in which both the fracture and the surrounding matrix participate in transport and reaction. Examples include fractured sandstones, granular or bioclastic carbonates, dolostones with intercrystalline porosity, silicified or dolomitizing carbonate rocks, and fractured mafic volcanic rocks with connected matrix porosity.

In this sense, the model should be viewed as a reduced-order representation of fracture–matrix reactive transport. Its purpose is to isolate the effects of fracture–matrix conductance contrast, reaction rates, and molar-volume change on coupled dissolution–precipitation dynamics.

The domain (see Fig. 1) has a constant thickness h_z, forming a quasi-2D microfluidic-like system. As mentioned before, the system has a single inlet, while the outlet extends along the lower boundary, with the outlet pressure set to $p_{\mathrm{out}} = 0$, which is lower than the inlet pressure p_{in}. A single fracture is introduced along the shortest path on the graph between the inlet and the outlet.

An extrinsic control is the forcing protocol: laboratory corefloods frequently impose constant total flow (pressure adjusted), whereas many subsurface systems evolve closer to constant pressure; as permeability drops under constant pressure, throughput collapses–accelerating clogging–even when chemistry is unchanged. Thus, we examine two driving protocols: constant pressure between the inlet and the outlet, and constant total flow through the system. In the constant-flow case, the total flow is maintained by rescaling p_{in} at each time step of the simulation. Periodic boundary conditions are applied along the left and right boundaries; the upper nodes that do not belong to the inlet are subject to impermeable (no-flux) boundary conditions.

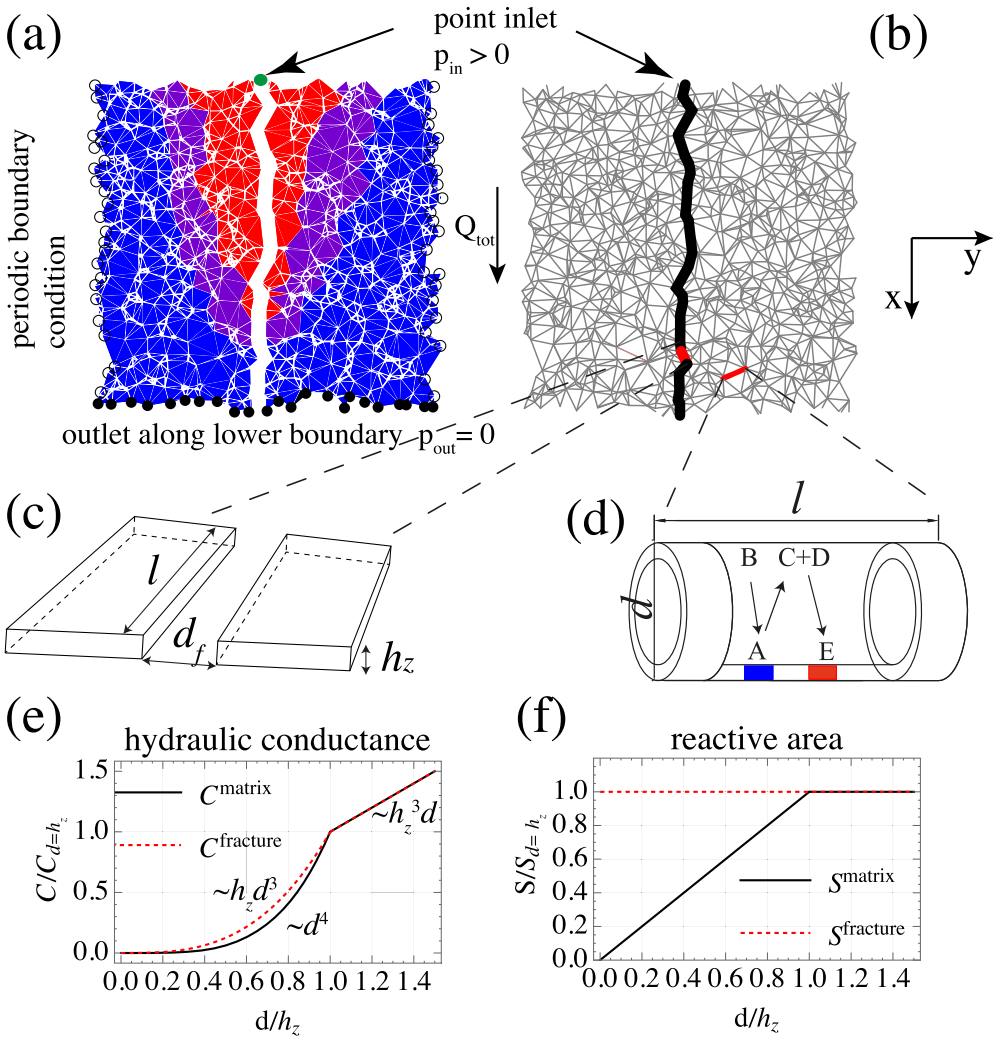

Fig. 1. Pore-network model. The porous medium is represented as a network composed of grains (panel a) and pores (panel b), where each pore body corresponds to a network node and each pore throat to an edge. Grains are composed of material A (shown in blue), material E (shown in red), or a mixture of both (shown in purple). The edges of the network (hereafter referred to as pores) can belong either to a fracture (panel c) or to the matrix (panel d). For fracture, the pore shape is approximated as a rectangular cuboid, with l denoting pore length, d_f its width, and h_z the height of the system (panel c). For matrix pores, the shape is assumed to be cylindrical (with length l and diameter d) as long as $d \leq h_z$; otherwise, it is approximated, similarly as before, as a rectangular cuboid. Both the hydraulic conductance (panel e) and the reactive surface area (panel f) depend on l, d, and the assumed pore geometry.

2.3. Flow, transport, and reactions in the network

To calculate flow through all pores and pressure at all nodes, we assume Hagen-Poiseuille flow in each element (see Fig. 1). We distinguish between network edges belonging to the matrix and those forming the fracture. For matrix pores, the geometry is approximated as cylindrical, and the hydraulic conductance, C_{ij}, is proportional to $\frac{d_{ij}^4}{l_{ij}}$ (Shah and London, 1978). Edges forming the fracture are assumed to have a rectangular cross-section, $d_{ij} \times h_z$, where h_z denotes the out-of-plane system width. For this geometry, the hydraulic conductance is approximated as $C_{ij} \sim \frac{d_{ij}^3}{l_{ij}}$, valid for $d_{ij} \ll h_z$ (Witherspoon et al., 1980). For both matrix and fracture pores, when the pore diameter exceeds the system width ($d_{ij} > h_z$), the conductance is estimated using $C_{ij} = \frac{\pi}{128\mu l_{ij}} d_{ij} h_z^3$, where μ denotes the viscosity of water. This corresponds to flow through a rectangular conduit of size $d_{ij} \times h_z$ in the limit $d_{ij} \gg h_z$. Note that the exact solution for Hagen-Poiseuille flow in a rectangular conduit involves an infinite series (Shah and London, 1978). For simplicity, we retain only the leading term and assume a sharp transition between cylindrical and rectangular geometries. In summary, the relationship between pressure drop and total flow through a given element is given by:

$$q_{ij}^{\text{matrix}} = \begin{cases} \frac{\pi}{128\mu l_{ij}} d_{ij}^4 (p_j - p_i) & \text{for } d_{ij} \leq h_z \\ \frac{\pi}{128\mu l_{ij}} d_{ij} h_z^3 (p_j - p_i) & \text{for } d_{ij} > h_z \end{cases}$$

$$q_{ij}^{\text{fracture}} = \begin{cases} \frac{\pi}{128\mu l_{ij}} d_{ij}^3 h_z (p_j - p_i) & \text{for } d_{ij} \leq h_z \\ \frac{\pi}{128\mu l_{ij}} d_{ij} h_z^3 (p_j - p_i) & \text{for } d_{ij} > h_z, \end{cases} \quad (5)$$

Combined with the mass conservation condition at each node, which ensures that the total flow through all its neighbor pores satisfies $\forall_i \sum_j q_{ij} = 0$, this results in a sparse system of linear equations for the nodal pressures, solved using the MUltifrontal Massively Parallel sparse direct Solver (MUMPS) (Amestoy et al., 2001, 2006). Once the pressure field is obtained, the flow through each element is computed using Eq. (5).

We assume that the characteristic time scales of flow and transport relaxation are much shorter than those of dissolution and precipitation (i.e., changes in d_{ij} and l_{ij}), because mineral-phase concentrations are

orders of magnitude higher than those of solutes in the fluid. This assumption allows us to employ a quasi-static approach, treating the flow and concentration fields as stationary at each time step (Lichtner, 1988). Furthermore, we neglect longitudinal diffusion along the pore axes but incorporate the transverse component into the reaction rates (Budek and Szymczak, 2012). Under these assumptions, and for fixed d_{ij} and l_{ij}, exact analytical solutions for the concentration fields of the reactants can be obtained (Budek and Szymczak, 2025).

Note that, similarly to the hydraulic conductance, the expression for the reactive surface area s_{ij}, as a function of d_{ij} and l_{ij} differs between fracture elements and matrix pores. We assume that the upper and lower surfaces are inert so we get $s_{ij}^{\text{fracture}} = 2l_{ij}h_z$ for a fracture. For matrix pores, the reactive surface area depends on d_{ij}: $s_{ij}^{\text{matrix}} = \pi l_{ij} d_{ij}$ for $d_{ij} \leq h_z$ and $2l_{ij}h_z$ otherwise.

Once the concentration field is known, the consumption or production of species A and E in each pore can be determined, corresponding to changes in the composition of neighboring grains

$$\Delta V^A = -\pi d \Delta t \int_0^l k_1 \frac{\chi_A}{\chi_B} \nu_A c_B(x) dx, \tag{6}$$

$$\Delta V^E = \pi d \Delta t \int_0^l k_2 \chi_E \nu_E c_C(x) dx. \tag{7}$$

Assuming uniform distribution of the dissolved A and precipitated E within each pore, we can update the geometric parameters d_{ij} and l_{ij} accordingly. A detailed derivation can be found in (Budek and Szymczak, 2025). Note that the simulation time step, Δt, is chosen dynamically so that, in each step, for no grain does the change $\Delta V_{A/E}/V(t=0)$ exceed 1%.

2.4. Simulation procedure

At the beginning of the simulation, the entire system consists solely of material A, depicted in blue in Fig. 1a. Water containing species B is injected at the inlet. The system height is taken to be on the order of the mean pore spacing ($h_z = l_0$), and the time unit, τ, is defined as the time needed to inject the initial pore volume of B, excluding the fracture.

Each simulation step consists of the following stages:

1. Solving for the pressure field at the nodes,
2. Computing flow rates in the pores,
3. Evaluating reactant concentrations at the nodes,
4. Updating the geometry, including pore diameters, pore lengths, and grain volumes and compositions,
5. Adapting the time step and performing pore merging.

The simulation continues until a given time ($t_{\max} = 33\tau$). If clogging is severe and the pressure required to sustain the constant flow exceeds 10^3 its initial value, the simulation is terminated earlier and interpreted as complete clogging of the system. In the case of constant inlet pressure conditions, the simulation is terminated if the total flow rate drops below 0.001 of its initial value.

To ensure numerical stability, pores with diameters below a certain threshold ($d < 0.01 d_0$) are removed, reflecting the physical loss of connectivity due to severe clogging. Conversely, in regions of intense dissolution, grain volumes may become very small, and the imposed connectivity between pores and grains may no longer be physically realistic (a small grain may artificially block access to a larger one). To address this issue, we introduce a merging procedure: grains whose volume falls below 20% of their initial value (corresponding roughly to a halving of their length) are merged with neighboring grains, thereby modifying the network topology. Importantly, this procedure conserves the total mass of species A and E, the reactive surface area, as well as the local hydraulic conductance. During the merging process, three pores are replaced by a single pore with parameters d and l selected to preserve the reactant area of the vanishing pores and to maintain a local conductivity (see Supplementary Materials).

2.5. Dimensionless numbers

For a given initial geometry, the system's evolution is fully determined by three dimensionless parameters. The first is the Fogler number, Fo, a dimensionless precipitation-to-dissolution rate ratio (Budek et al., 2026),

$$\text{Fo} = \frac{k_2}{k_1}, \tag{8}$$

which quantifies the relative dominance of precipitation over dissolution processes (Budek and Szymczak, 2025).

The evolution of the pore space strongly depends on whether the reaction leads to a net increase or decrease in the solid volume. Thus, we introduce the second parameter Γ, which relates the volume of solid produced by precipitation of E to the volume of solid removed by dissolution of A:

$$\Gamma = \frac{\chi_E \nu_E}{\chi_A \nu_A}, \tag{9}$$

where ν_E and ν_A are the molar volumes of the precipitating and dissolving phases, respectively, and χ_E and χ_A account for the corresponding stoichiometric factors. When $\Gamma > 1$ (e.g., mineral carbonation of mafic-ultramafic rocks; serpentinization of olivine or aragonite - calcite replacement) void space tends to decrease and pathways seal; conversely, when $\Gamma < 1$ (e.g., replacement of calcite by quartz during chertification, calcite - dolomite, gypsum - anhydrite or albite - kaolinite replacement) porosity can reopen (Putnis, 2021). This helps explain why silica-cemented intervals often act as barriers, while some dolomitized zones remain transmissive (Hollis et al., 2017).

The third parameter is the global Damköhler number, defined as

$$\text{Da} = \frac{\pi l_0 d_0 k_1(d_0)}{q_0}, \tag{10}$$

where l_0 is the mean distance between neighboring nodes, and d_0 and q_0 denote the initial diameter of matrix pores and the initial mean flow through those pores (in absence of the fracture), respectively. Note that in the present study, for the sake of clarity, the system width is kept constant, as is the pore density per unit length, and the initial flow rate is adjusted to achieve the desired value of the Damköhler number, $Q(t=0) = N_y \frac{\pi k_1 l_0 d_0}{Da}$.

The geometry of the system, apart from the initial node positions, is further characterized by two additional parameters. The first is the initial porosity, φ_0, which is uniquely determined by the initial pore diameter, d_0, through $\varphi_0(d_0) = 1 - \frac{(2-d_0^2\pi)^{3/2}}{2\sqrt{2}}$. This relation is derived for an ideal hexagonal network (for details, see Budek and Szymczak, 2025).

The second geometrical parameter is the initial fracture-to-matrix hydraulic conductance ratio, Cr, which quantifies the initial contrast in flow conductance between the fracture and the surrounding matrix. It depends on the ratio of the initial fracture and matrix pore diameters. The initial diameter of matrix pores is assumed uniform and equal to $d_0 < h_z$, while the corresponding pore lengths vary due to the random placement of nodes. The initial fracture aperture, d_0^{f}, is also uniform but differs from d_0. Accordingly, the initial fracture-to-matrix conductance ratio is given by

$$\text{Cr} = \begin{cases} \frac{(d_0^{\text{f}})^3 h_z}{d_0^4} & \text{for } d_0^{\text{f}} \leq h_z \\ \frac{d_0^{\text{f}} h_z^3}{d_0^4} & \text{for } d_0^{\text{f}} > h_z. \end{cases} \tag{11}$$

3. Results

3.1. Impact of the fracture

Let us investigate the impact of fracture on the evolution of the system. Simulation results for a system consisting of 100 × 200 nodes with various fracture sizes are presented in Fig. 2. The default reaction parameters, Da = 0.1, $\Gamma = 1$, and Fo = 1, were used and the total

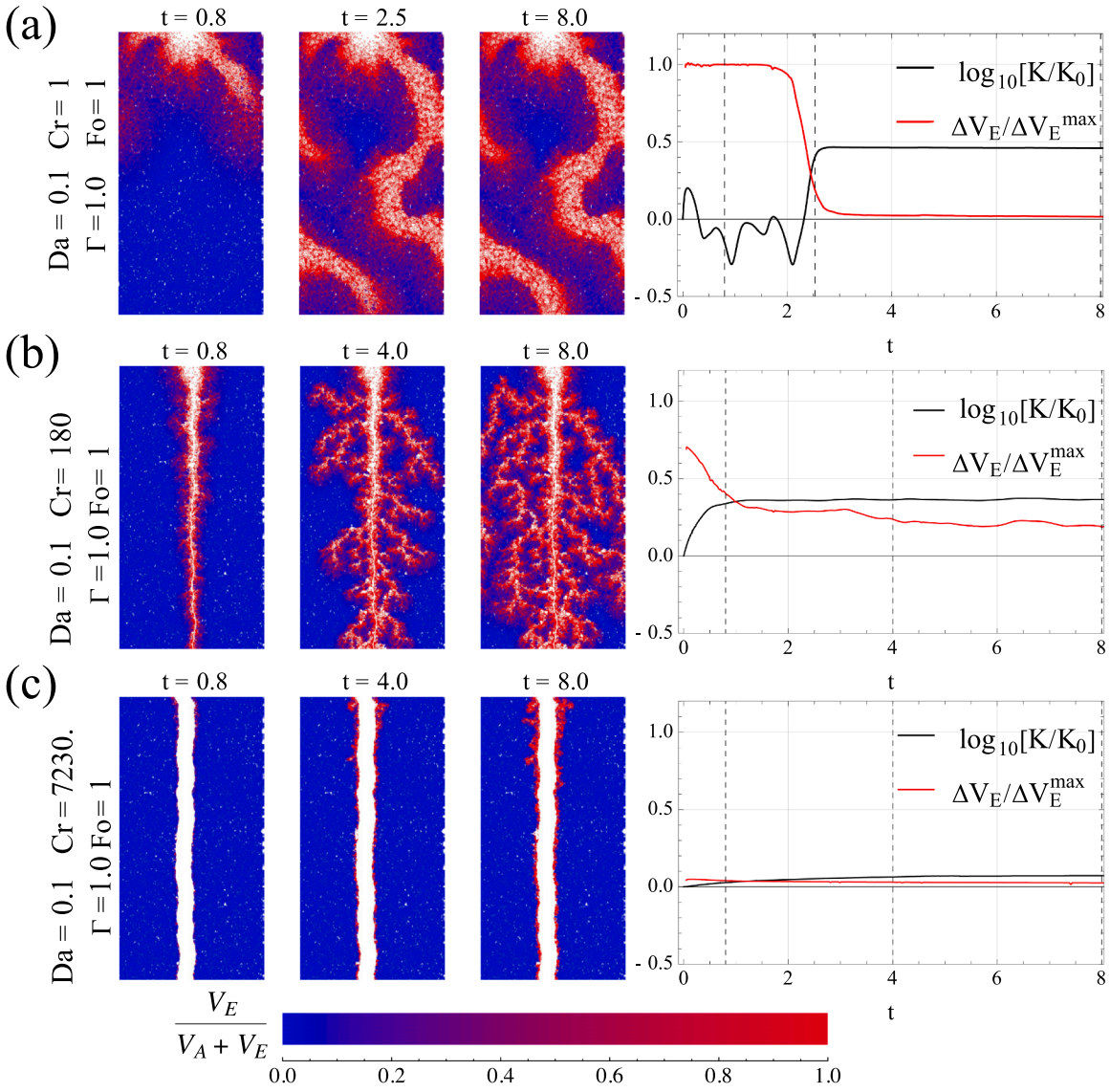

Fig. 2. Simulation results for different fracture-to-matrix conductance ratios: Cr = 1 (panel a), Cr = 180 (panel b), and Cr = 7230 (panel c). Three stages of system evolution are presented, where blue denotes grains consisting of material A, red represents grains consisting of material E, and empty space is shown in white (see the color bar at the bottom). The images are accompanied by normalized permeability and deposition rate over time. Vertical dashed lines indicate the moments of image capture shown on the left. The default simulation parameters were used: $N_x \times N_y = 100 \times 200$, Da = 0.1, $\Gamma = 1$, Fo = 1, and $\varphi_0 = 15\%$. Depending on the fracture size, we observe three distinct regimes: wormholing (no fracture), branching (small fracture), and fracture dominance (large fracture).

flow rate through the system was kept constant. The initial porosity of the matrix was set to $\varphi_0 = 15\%$ and the total flow rate through the system was held constant. Fig. 2(a) shows the time evolution of a system without a fracture (Cr = 1). It includes plots of the normalized permeability, $K(t)/K_0 = \frac{\Delta P^0_{\text{in}}}{\Delta P_{\text{in}}(t)}$, where K_0 denotes the initial permeability of the system. Alongside, the normalized precipitation rate is plotted, $\frac{\Delta V_E(t)}{\Delta V_E^{\max}} = \frac{V_E(t+\Delta t) - V_E(t)}{\Delta t Q^0_{\text{tot}} c_B^{\text{in}} \nu_A \chi_A / \chi_B}$, which is defined as the fraction of precipitate deposited at a given time relative to the maximum possible deposition from the injected reactants, $\Delta V_E^{\max}$. Here, Q^0_{tot} is the total flow through the system. As long as the total system flow and the inlet concentration of species B remain constant, $\Delta V_E^{\max}$ also remains constant.

In the case without fractures, we observe the growth of a single wormhole in the system, although secondary reactions distort both its shape and growth direction. Instead of the straight, regular wormhole that would develop in the absence of precipitation, a bulbous structure forms, meandering through the system at an angle. This behavior results from the ongoing competition between dissolution and precipitation reactions. Precipitate accumulates in front of the most active part of the dissolution pattern, either halting its growth or forcing it to seek new pathways toward the system outlet. Consequently, the total permeability of the system oscillates over time until breakthrough occurs. Permeability oscillations in dissolution-precipitation systems have been reported both experimentally (Rege and Fogler, 1989; Singurindy and Berkowitz, 2003) and in numerical simulations (Budek and Szymczak, 2025). In contrast to typical wormhole behavior, where B gradually decreases along the channel and a characteristic maximum length emerges, the presence of precipitation alters the dynamics: the wormhole becomes surrounded by grains fully transformed into material E, so B concentration decreases only near the actively growing tip. This effect leads to the emergence of self-replicating patterns that propagate through the system.

Notably, after the wormhole tip reaches the system's outlet, both the permeability and the precipitation rate stabilize. After breakthrough, almost all reactants are flushed out of the system as the flow becomes focused solely in the wormhole, where dissolution ceases because the

surrounding grains consist entirely of secondary material E. As a result, until breakthrough, the deposition rate remains close to unity since all reactants are consumed at the tip of the growing wormhole. After breakthrough, however, the deposition rate drops to nearly zero. The final permeability is approximately 2.5 times higher than the initial value, as the wormhole serves as a flow channel with lower hydraulic resistance.

The evolution of the system with a small fracture (conductance ratio 180) is presented in Fig. 2b. Initially, most of the flow is concentrated within the fracture, leading to a rapid increase in permeability, which soon reaches a plateau. This early growth of K is primarily due to the widening of the fracture. Once most of material A in the fracture vicinity is replaced by E (the initial stage of fracture rebuilding), permeability stabilizes, and precipitation starts to counterbalance dissolution by partially clogging the preferential flow path. Unlike the no-fracture case, stabilization does not coincide with complete flushing of reactants from the system. The deposition rate is lower than in the no-fracture case and decreases over time, but remains significantly above zero throughout the entire simulation. Following the initial replacement of A by E near the fracture (up to $t = 0.8$) and the attainment of a steady K, intense side branching occurs, distributing the precipitate away from the fracture (see video M1).

The side-branching that enables deep deposition of E within the matrix arises from reactive-infiltration instability: the transverse flow into the matrix is not distributed uniformly but instead concentrates along paths that compete with one another for the available flow (Chadam et al., 1986; Ortoleva et al., 1987). In replacement systems, an analogous instability develops when a locally more porous–and thus more permeable–intermediate zone forms between the dissolution and precipitation fronts, which focuses flow and promotes finger growth (Kondratiuk et al., 2017). The side-branching observed here is similar to the early stages of wormholing in rectangular geometry (linear inlet), where many channels nucleate and compete before wavelength selection and coarsening set in (Szymczak and Ladd, 2006; Cohen et al., 2008; Cabeza et al., 2020). Additionally, partial fracture clogging further redistributes flow into the matrix, reinforcing branch initiation. The number and thickness of the branches depend on Da, which governs the instability wavelength in reactive-infiltration systems. Note that at late times the deposition rate stabilizes at around 5% and remains at a similar level until almost the entire system has been transformed from A to E (see Supplementary Fig. S3).

Side branching of the dominant pattern, in which branches develop in the transverse direction, is observed in a variety of systems governed by a Laplacian field (so-called Laplacian growth), for example during dendrite formation (Couder et al., 2005) or viscous fingering on a rectangular grid (Budek et al., 2015). This behavior suggests that the emergence of such structures is universal, provided geometric constraints are imposed, and that it is controlled by the interaction between the growing pattern and the Laplacian field.

Let us now consider a system with a larger fracture, with a conductance ratio of approximately 7000 (see Fig. 2c). In this case, almost all the flow is concentrated within the fracture. Following the initial transformation of grains near the fracture (from A to E), the permeability stabilizes rapidly, remaining close to its initial value. The deposition rate is extremely low from the outset and continues to decrease over time. This dominance of the fracture results in effective passivation, as all grains in its vicinity are quickly converted into material E, which inhibits dissolution and slows further deposition.

In summary, we can observe three different regimes of system evolution depending on the fracture size: wormholing (no fracture), side-branching (small fracture), and fracture dominance (large fracture). Additionally, supplementary materials include a discussion of the impact of system length (see Fig. S1 and S2), concluding that no qualitative differences are observed in either the wormholing or side-branching regimes, even in simulations performed on larger networks and over longer times.

3.2. Optimal fracture sizes and branching mechanisms

We now quantitatively analyze the deposition properties as a function of fracture size. The total E deposition and deposition depth for different conductance ratios and at different times are presented in Fig. 3a,b. The deposition depth is defined as the mean transverse distance from the fracture centerline to the centers of grains containing at least 50% of phase E, normalized by L_y. The results have been averaged over 30 realizations with different initial positions of the nodes. The longer the simulation lasts, the more pronounced the positive impact of the fracture on the total amount of deposition becomes. The optimal fracture-to-matrix conductance ratio lies between 50 and 1000, with the maximum for both total deposition amount and deposition depth occurring at Cr ≈ 100. For Cr larger than 1000, both deposition depth and total deposition volume drop abruptly as the system shifts toward the fracture-dominance regime associated with fracture passivation.

Efficient deposition of E for Cr ≈ 100 in the presence of a fracture is associated with intense branching. To elucidate the branching mechanism, conductance along the fracture was plotted at different time steps for Cr = 180 (see Fig. 3c). The permeability of the fracture increases intensely only near the inlet, but deeper in the system there are regions where partial clogging of the fracture occurs - its conductance drops below the initial value. This partial clogging reinforces the redistribution of flow into the matrix, resulting in branches that initially grow perpendicular to the fracture and later bend while searching for the shortest path to the system outlet. As a result, we can deposit material E deep into the system, and the total amount of deposited material exceeds that in the no-fracture scenario.

To quantify the impact of fracture partial clogging on system evolution, we estimate the normalized reduction in fracture-matrix conductance ratio due to clogging, using the relation,

$$\mathrm{Cr}'/\mathrm{Cr} = \left(1 - f(d_0)\Gamma\left(\frac{(\Gamma-1)\mathrm{Fo}+1}{\mathrm{Fo}\Gamma}\right)^{\frac{\mathrm{Fo}}{\mathrm{Fo}-1}}\frac{l_0}{d_f}\right)^3, \tag{12}$$

derived in the Supplementary Material S3, where Cr′ is the fracture-matrix conductance ratio due to clogging and $f(d_0) = \left(\sqrt{3} - \frac{\pi d_0^2}{l_0^2}\right)^{3/2}/(2\sqrt[4]{3})$ is a factor depending on initial porosity. The clogging effect weakens as the initial fracture aperture increases. For a representative case with an initial porosity of 15%, Γ = 1, and Fo = 1, this simplifies to $\frac{\mathrm{Cr}'}{\mathrm{Cr}} \approx (1 - 1.2\mathrm{Cr}^{-1/3})^3$. The threshold value of Cr at which clogging fully compensates the fracture-matrix conductance contrast, estimated by solving $(1 - 1.2\mathrm{Cr}^{-1/3})^3 = 1/\mathrm{Cr}$, is $\mathrm{Cr}_{th} \approx 10$. This agrees with Fig. 3a, where fractures with Cr < 10 have little influence or even reduce precipitation by shortening the wormhole. For the reference case (Cr = 180), the predicted maximal conductance reduction is Cr′/Cr ≈ 0.49, consistent with the results in Fig. 3c.

Local partial clogging within the fracture plays a major role for small and medium Cr, while its effect vanishes for larger values. To determine the upper limit of Cr for which side branching can still occur, we examine the initial flow distribution before any reaction takes place. As shown in the Supplementary Material S4, the flow rate within the large fracture, q_f, decays exponentially along the downstream distance along the fracture until it reaches an asymptotic value set by the fracture-to-matrix conductance ratio:

$$\frac{q_f}{Q_{\mathrm{tot}}} = \left(1 - \frac{q_f^\infty}{Q_{\mathrm{tot}}}\right)e^{-x/\lambda} + \frac{q_f^\infty}{Q_{\mathrm{tot}}}. \tag{13}$$

The asymptotic fracture flow rate, q_f^∞, satisfies $Q_{\mathrm{tot}} = 2N_y q_m^\infty + q_f^\infty = 2N_y q_f^\infty/\mathrm{Cr} + q_f^\infty$, where q_m^∞ is the characteristic flow rate through a matrix pore far from the inlet, and the system width spans $2N_y$ matrix pores. Hence, $\frac{q_f^\infty}{Q_{\mathrm{tot}}} = \frac{\mathrm{Cr}}{\mathrm{Cr}+2N_y}$ and $\frac{q_m^\infty}{Q_{\mathrm{tot}}} = \frac{1}{\mathrm{Cr}+2N_y}$.

For the reactive-infiltration instability to develop, the reactant penetration length must be comparable to the pore length or larger. Approximating horizontal flow from fracture to the matrix as $q_m^\perp \approx q_m^\infty$ and

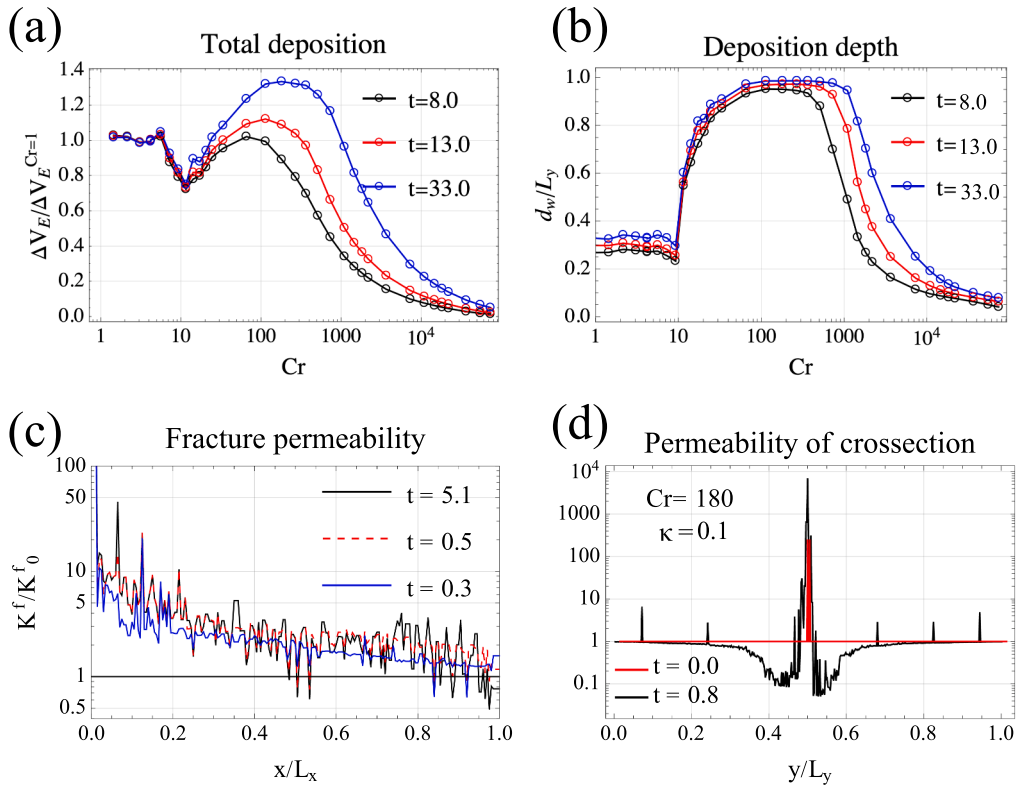

Fig. 3. Panel (a) depicts the deposition efficiency (total volume of material E) as a function of the fracture-to-matrix conductance ratio, Cr, for different total simulation times, t, where time unit is equal to time required to inject initial pore volume of species B. Note that the deposit volume is normalized by the volume of E deposited in the no-fracture scenario. Panel (b) depicts deposition depth as function of Cr for three different times. Additionally, panel (c) presents the time evolution of local conductance along the fracture: while the inlet part of the fracture opens intensively, the conductance of the remaining section can oscillate, occasionally dropping below its initial value, which facilitates side branching. The passivation mechanism for small Fo is analyzed in panel (d), where the local conductance distribution along the horizontal axis at $x = 0.5$ is plotted for two different times for Fo = 0.1.

substituting into the local Damköhler number yields $\mathrm{Da}_{\mathrm{matrix}} = \mathrm{Da}\frac{q_0}{q_m^{\perp}} \approx \mathrm{Da}\frac{\mathrm{Cr}+2N_y}{2N_y}$, which becomes unity for Cr ≈ 1800. This value is consistent with Fig. 3ab, where for $\mathrm{Cr} > 10^3$ the branching effect disappears. In summary, when $10 \lesssim \mathrm{Cr} \lesssim 10^3$, the fracture is sufficiently large to be significant, yet not so large that $\mathrm{Da}_{\mathrm{matrix}} > 1$; in this regime, partial clogging further increases $\mathrm{Da}_{\mathrm{matrix}}$.

3.3. *Regime map: impact of* Da *and* Fo

The dissolution and precipitation penetration lengths, L_B and L_C, which play a key role in controlling the system dynamics, depend on the Damköhler number (Da) and the Fogler number (Fo). In the absence of a fracture, these relationships are given by $L_B = l_0/\mathrm{Da}$ and $L_C = l_0/(\mathrm{FoDa})$. The presence of a fracture shortens the penetration length within the surrounding matrix while extending it along the fracture, where the flow is concentrated. The extent of this shift depends strongly on the fracture aperture, quantified by the conductance ratio Cr. In the following, we examine how these reaction-related parameters influence the temporal evolution of the system.

The final stages of evolution for simulations on a network consisting of 100×200 nodes for different values of Da and Fo are presented in Fig. 4a. Total time of a simulation was set to $t = 6\tau$. As before, the initial matrix porosity is set to $\varphi_0 = 15\%$, and a single fracture with Cr = 180 is added in the middle of the system. The parameter Fo affects the shape of emerging pattern in a significant way. For large Fo, precipitation occurs much faster than dissolution and takes place in situ, in the same pores where dissolution previously occurred. Since $\Gamma = 1$ and the instantaneous transformation A → E does not alter local porosity, reactive-infiltration instability weakens, leading to the formation of a uniform front. As a result, instead of branching, we observe a carrot-like, regular shape of the precipitate around the fracture. As shown in Supplementary Materials S3, the uniform replacement regime behaves similarly in the absence of a fracture (Budek and Szymczak, 2025), although the presence of the latter enables deeper deposition of the precipitate, whereas without a fracture, material E would accumulate primarily near the inlet (see video M2).

For intermediate values of Fo ∼ 1, as mentioned earlier, intensive side branching of the pattern is observed. Since the penetration lengths of the dissolving and precipitating reactants, L_B and L_C, are similar and greater than the length of a single pore, the competition between these two processes is very strong. On the other hand, for small Fo, precipitation and dissolution are spatially separated (Budek and Szymczak, 2025), as the precipitate has a chance to travel deeper into the system before being deposited ($L_c > L_B$). As a result, rapid fracture passivation occurs, accompanied by permeability stabilization and a decline in deposition to almost zero. This is a consequence of the emergence of a thick layer of precipitate at some distance from the fracture–this clogged region inhibits flow into the matrix. Note that for smaller Da, this passivation region occurs further from the fracture; thus, at the beginning of the simulation, intense fracture widening is observed. However, once all of mineral A ahead of the passivation region has dissolved, no further chemical reactions occur in the system.

To elucidate this behavior, we analyzed the conductance profile across the cross-section (at $x = 0.5N_x$) at different time steps for Fo = 0.1 and Da = 1 (see Fig. 3d). At the beginning of the simulation, the conductance of the matrix was uniform, with only the pores forming the fracture exhibiting high initial conductance (red peak). After a short

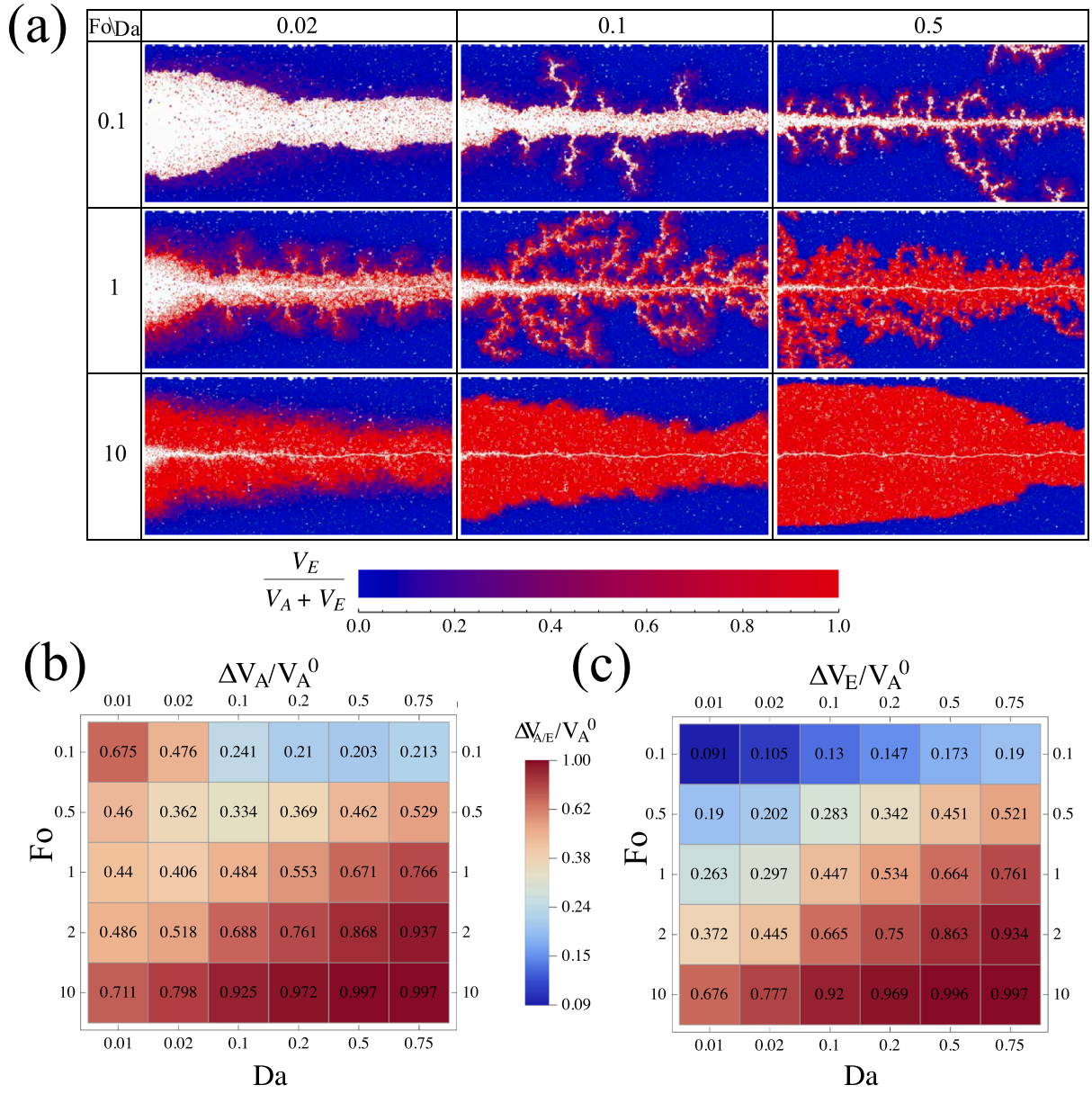

Fig. 4. Dissolution and precipitation patterns around the fracture for different Damköhler numbers (corresponding to different flow rates through the system) and different Fogler numbers, Fo, are presented in panel (a). We observe three distinct regimes depending on Fo: passivation for small Fo, characterized by a large spatial separation between dissolution and precipitation; branching for medium Fo, where the separation is smaller; and uniform replacement for large Fo, where precipitation occurs 'in situ' without spatial separation. The effectiveness of A dissolution and E deposition are presented in panel (b) and (c), where the total volume of dissolved A (or deposited E) are shown for wide range of parameters Da and Fo. Both ΔV_A and ΔV_E are expressed as fractions of the total initial volume of solid material. Results are presented for $t = 6\tau$ and have been averaged over 30 realizations.

time ($t = 0.8\tau$), the conductance distribution changes. While conductance increases around the fracture, it simultaneously drops significantly at some distance from it. This is the region that, on one hand, has not yet undergone much dissolution, but has accumulated a large amount of precipitate. In contrast, the conductance of the fracture ($y/L_y \approx 0.5$) increases significantly as dissolution dominates there.

In summary, we observe three distinct pattern formation regimes depending on the relative rate of precipitation to dissolution, Fo. For fast precipitation, we obtain uniform A → E replacement; for intermediate values of Fo, side branching occurs; and for slow precipitation, fracture passivation dominates.

The Damköhler number, Da, also has a significant impact on pattern formation, primarily influencing the diffuseness of the patterns. It determines both reactant penetration lengths ($L \sim 1/\mathrm{Da}$). For small Da (long penetration length), patterns become more diffuse, and more reactants are flushed out of the system. On the other hand, for short penetration lengths (large Da), the edges of patterns become sharper. In this case, branches are thinner, more numerous, and begin to merge (see Da = 0.5 and Fo = 1). Notably, for large Da, the passivation effect weakens, as individual side branches can still continue its growth. This results from the shorter distance between the fracture and the clogged area as well as the thinner layer of the latter – both consequences of shorter precipitation penetration length.

The effectiveness of A dissolution and E deposition is presented in Fig. 4b and c, respectively, where the total volume of dissolved A (or deposited E) are shown for wide range of parameters Da and Fo. Both ΔV_A and ΔV_E are expressed as fractions of the total initial volume of solid material. The total volume of dissolved A is not a monotonic

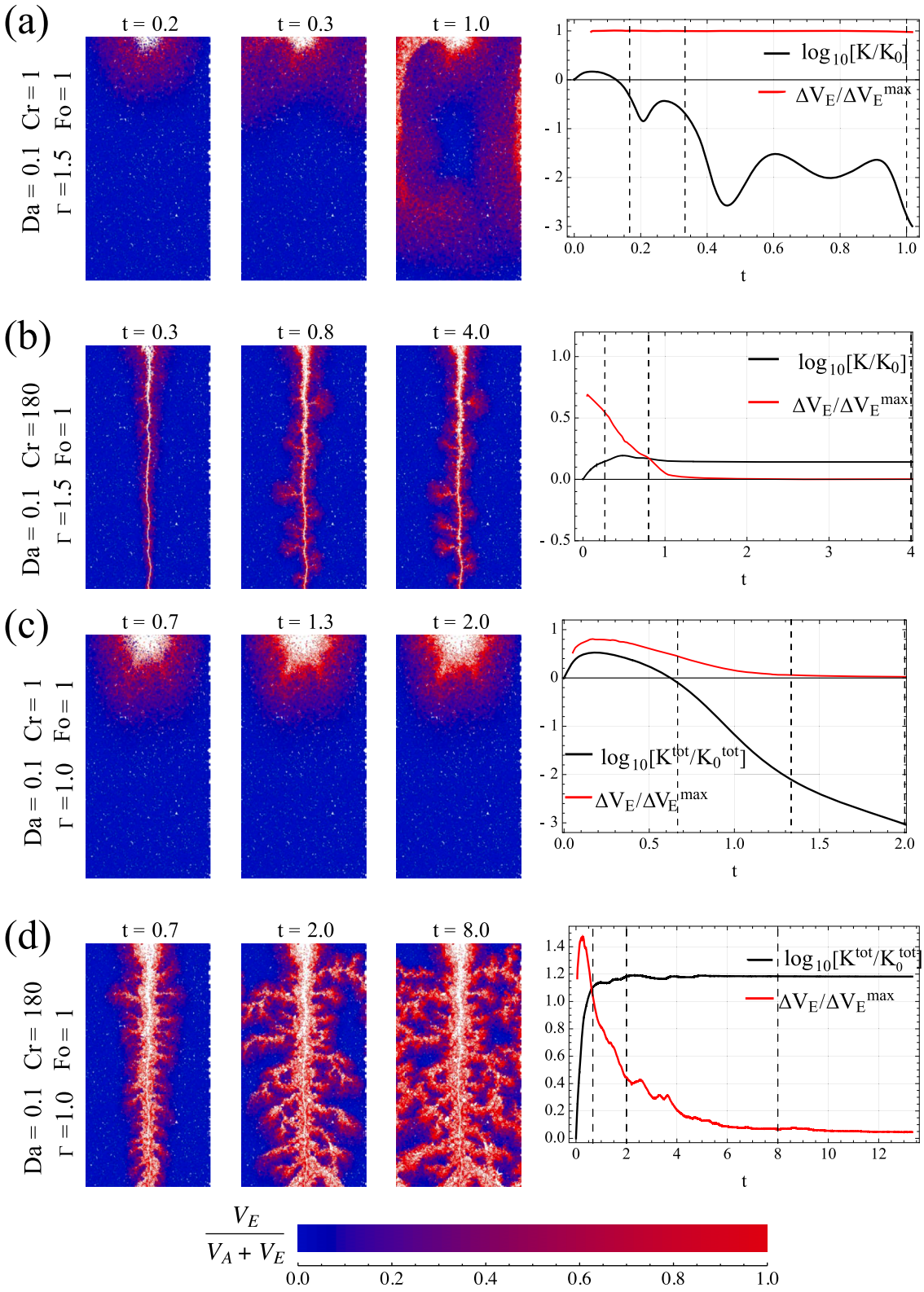

Fig. 5. Clogging vs. non-clogging: Comparison between no-fracture and fracture scenarios for a large molar volume ratio of secondary to primary rock (panels a and b) and for the default set of simulation parameters but with a constant inlet pressure (panels c and d). Three stages of system evolution are presented, where blue denotes grains consisting of material A, red represents grains consisting of material E, and empty space is shown in white (see the color bar at the bottom). The images are accompanied by normalized permeability and deposition rate over time. Vertical dashed lines indicate the moments of image capture shown on the left.

function of either Fo or Da. For small values of Fo and Da, the penetration length of the precipitating reactant (L_C) exceeds the system length, and intense flushing of the precipitant promotes efficient dissolution, as it is not hindered by precipitation. As Fo and Da increase, the competition between dissolution and precipitation becomes stronger, resulting in thinner dissolution patterns and a reduced total volume of dissolved primary material. Finally, for the largest values of Fo and Da, the reactants are no longer flushed out as both L_B and L_C are much smaller then system length. Additionally, intense side branching broadens the patterns. As a result, ΔV_A increases significantly, reaching its maximum in the regime of uniform A-to-E replacement. The most efficient deposition of material E in the system also corresponds to this uniform replacement regime, which occurs at high Fo. Additionally, large values of Da prevent flushing of the reactants and further increase the amount of E that can be deposited (see Fig. 4c). Consequently, the maximum E deposition is observed for Da = 0.75 and Fo = 10, where ΔV_A and ΔV_E reach their plateau as the system switches to the replacement regime in which all material A is replaced by E.

3.4. Clogging

Dissolution accompanied by precipitation can lead to total clogging of the system. The system is prone to clogging when the solid volume produced by precipitation exceeds the solid volume removed by dissolution, $\Gamma > 1$. Simulation results for $\Gamma = 1.5$, Fo = 1, and Da = 0.1 are presented in Fig. 5, where panel (a) depicts the scenario without a fracture and panel (b) – with a fracture. As before, the initial matrix porosity is set to $\varphi_0 = 15\%$ and Cr = 180. As predicted, a large Γ leads to rapid clogging of the system.

What is striking is that the presence of a small fracture (Cr = 180) prevents the system from clogging. Even though the solid volume produced by precipitation exceeds that removed by dissolution, the permeability of the system grows over time. The characteristic side branching is also present, although the branches are thinner and shorter than for $\Gamma = 1.0$ (see Fig. 2b). The deposition rate drops to zero during the simulation but the system remains far from being clogged, with permeability staying constant at a level above its initial value. In Supplementary Material S1, we show that the system size does not affect this clogging/non-clogging behavior. Note that, according to Eq. (12), for $\Gamma = 1.5$ and Fo = 1, the minimum Cr below which the fracture becomes fully clogged is $\mathrm{Cr}_{\mathrm{thr}} \approx 90$, which is in agreement with the presented results. This relation is largely insensitive to the system size.

The presence of a fracture plays a crucial role, as it modifies the distribution of reactants within the system. The fracture channels the flow along a single pathway while diverting significant amounts of material E to its sides, in contrast to the downstream transport observed in spontaneously growing wormholes, whose growth is accompanied by intense lateral clogging of the surrounding area. The influence of system anisotropy on pattern development was also demonstrated by Roded et al. (2021), who showed that the tendency of wormholes to branch depends on the size of the perpendicular connections between fractures.

Once the fracture becomes partially clogged (see Fig. 3c), intense side branching develops, distributing the precipitate deep into the system and away from the main conduit. In contrast, in the absence of a fracture, most of the precipitate is deposited downstream of the wormhole, leading to its effective clogging.

Clogging can also become severe under constant inlet pressure, in contrast to the earlier constant-flow setup where pressure was adjusted. As shown in Section 3.1, the growth of a single wormhole is accompanied by intense permeability oscillations, during which permeability can drop significantly below its initial value (see Fig. 2a). Under constant pressure boundary conditions, a drop in permeability would be accompanied by a reduction in total flow through the system, decreasing the reactant penetration length (both L_B and L_C). This would make clogging around the wormhole tip more effective, further decreasing permeability and flow. As a result, the total flow through the system would fall below $Q_{tot}^{\min} = 10^{-3} Q_{tot}^{0}$, which we interpret as complete clogging of the system. Fig. 5c indeed shows rapid clogging of the system under a constant pressure condition.

Surprisingly, in the presence of a fracture, the permeability does not drop below its initial value (see Fig. 5d). Consequently, under constant pressure, the total flow increases during the simulation, extending the reactant penetration length (see video M3). As a result, the system does not become clogged, and a highly branched pattern develops, which is more diffuse than that obtained under constant-flow conditions (compare Figs. 2b and 5d). The shift in pattern shape corresponds to a shift to smaller Da in Table 4a, reflecting the longer penetration lengths of B and C. This is consistent with the fact that, in the presence of a fracture, the total flow through the system increases.

The contrast between systems without and with a fracture is striking. In the absence of a fracture, the system clogs rapidly, yielding only a limited amount of precipitate. With a fracture, however, clogging does not occur, and the total precipitate exceeds that observed under constant-flow conditions. Here, side branching, together with increased penetration lengths, distributes the precipitate more effectively, preventing clogging and sustaining flow throughout the system.

4. Discussion

This study demonstrates that fractures exert a first-order control on the coupled dynamics of dissolution and precipitation in reactive porous media. Beyond simply accelerating flow, fractures fundamentally reshape reaction patterns by enabling regimes of passivation, side branching, and uniform replacement. Partial clogging within fractures redirects flow into the matrix and drives side-branching instabilities that distribute precipitation deep into the system. In contrast, spatial separation between dissolution and precipitation promotes passivation, while faster precipitation relative to dissolution produces more uniform transformation of the rock matrix. Two controls emerge consistently: (i) the precipitation-to-dissolution rate ratio (Fogler number, Fo), which governs regime selection (passivation → branching → replacement), and (ii) fracture aperture (or the fracture-to-matrix conductance ratio, Cr), which controls the degree of focusing and export of reaction products. We find that an optimal fracture-to-matrix conductance ratio maximizes secondary mineral deposition, whereas overly dominant fractures suppress reactions through rapid passivation. Furthermore, fractures can substantially mitigate clogging by redistributing precipitates into side branches, a behavior observed under both constant-flow and constant-pressure boundary conditions. The observed side branching, passivation, and permeability evolution are qualitatively consistent with experimental observations reported in fractured carbonate systems and recent microfluidic studies of coupled dissolution-precipitation processes (Rege and Fogler, 1989; Singurindy and Berkowitz, 2003; Garcia-Rios et al., 2015; Nisbet et al., 2025). However, direct experimental studies explicitly investigating coupled dissolution-precipitation dynamics in fracture-matrix systems remain limited, representing an important direction for future work.

Field observations report dynamics akin to those described here. For example, in the Suez Rift, Egypt, hydrothermal dolomitization evolved from early, fracture-fed fluids leaking laterally into beds–producing widespread, bed-parallel dolomite–to later flow that localized within the fault plane, where massive dolomite cement accumulated and sealed the fracture zone (Hollis et al., 2017). This case illustrates how fracture pathways can first drive matrix replacement and subsequently transition to cement-filled conduits as fracture aperture and conductance change.

Consistent field evidence comes from a tectonically active salt basin (Koeshidayatullah et al., 2022), where dolomitization fronts coevolve with fracture corridors: dolomite stoichiometry and cation ordering increase toward dolomite cores, and early seawater-derived, fabric-retentive dolomite grades upward into fracture-controlled, fabric-destructive hydrothermal dolomite. The same study links front re-

treat/termination to a decline in the dolomitizing capacity of Mg-rich fluids and shows later, hotter pulses localizing along dolostone-limestone boundaries. These mapped transitions–from distributed bed-parallel replacement to fracture-focused cementation and sealing–echo our predicted shift from uniform replacement to passivation as conductance and chemistry evolve.

Silicification provides a complementary case – silica-bearing fluids migrating along fractures both replace carbonate matrix with microcrystalline quartz/chalcedony and fill open space, producing chert/jasperoid bodies and sealed veins. Numerous field studies report fracture-parallel silicification halos with textures diagnostic of coupled dissolution-precipitation (You et al., 2018; Dong et al., 2018; Pisani et al., 2022). For example, in the Tarim Basin, You et al. (2018) documented two fracture-related silicification styles: (i) pervasive replacement of limestone adjacent to fractures by microcrystalline quartz, and (ii) silica cements that line and locally fill fractures (chalcedony/quartz). The result is partially silicified wall rock flanking quartz-lined conduits: fracture-fed silica can create secondary porosity where carbonate dissolves, while simultaneously sealing pores and fractures where silica precipitates.

In shallow hydrothermal systems, fracture-hosted epithermal veins often show alteration and replacement halos propagating into the wall rock. For instance, at many carbonate-hosted epithermal deposits, limestone adjacent to quartz-calcite veins is selectively replaced by silica or sulfide minerals, creating a metasomatic front (jasperoid or carbonate-replacement ore) extending outward from the vein (Wilkinson et al., 2005; Simpson and Christie, 2019; Madondo et al., 2021). These field observations (alteration halos, mineralogical gradients, and lateral zonation of mineral assemblages) demonstrate that fracture-fed fluids not only deposit vein fillings but also diffuse into the surrounding rock, causing coupled dissolution-precipitation in the matrix.

These dynamics have also direct implications for subsurface applications. For carbon mineralization, this work suggests strategies for achieving more uniform and extensive trapping of CO_2 without severe clogging. Specifically, operating within parameter regimes that favor side branching or uniform transformation could promote widespread and stable mineral deposition. For in situ mining, the capacity of fractures to extend reaction volumes and deliver reactants deep into the matrix highlights opportunities to access larger rock domains. Deliberate precipitation of unwanted secondary minerals could be used to reinforce side-branching and stabilize flow paths, while target elements are mobilized and extracted through strategies that exploit the side-branching and replacement regimes identified here.

Finally, the identification of optimal fracture dimensions and governing dimensionless parameters provides a framework for site selection and engineered stimulation. By targeting fracture geometries and reaction conditions that enhance side branching and uniform precipitation, operators may better balance reactivity and permeability, maximizing efficiency while minimizing clogging. More broadly, this work demonstrates fractures as active regulators of coupled dissolution-precipitation dynamics, with direct relevance to both natural geochemical processes and engineered subsurface applications.

Several simplifying assumptions of the present model should be kept in mind when interpreting the results. First, the quasi-2D pore-network representation neglects the full geometric complexity of fully three-dimensional systems. While we expect the main regimes identified here–passivation, side branching, and uniform replacement–to persist in 3D media, the additional degree of freedom would likely modify the morphology of reactive pathways (e.g., increased tortuosity and branching) and shift the critical values of the Damköhler number, Fogler number, and fracture-to-matrix conductance at which regime transitions occur.

Second, the chemical model assumes linear reaction kinetics with constant rate coefficients, whereas real systems often exhibit nonlinear dependencies on species concentrations and coupled reaction pathways; incorporating such effects would likely shift the system's position within the regime diagram and could lead to spatial evolution of patterns along the flow direction. In the present framework, however, the Fogler number can also be interpreted as the ratio of the characteristic penetration lengths associated with precipitation and dissolution fronts. This suggests that regime emergence is governed primarily by the relative spatial separation between dissolution and precipitation zones, such that a generalized penetration-length ratio may remain a useful predictor even in more complex nonlinear reaction systems.

In addition, microscopic surface roughness is not explicitly resolved, as pore elements are idealized as smooth cylinders below the characteristic length scale l_0; however, effective roughness emerges at larger scales through imposed fracture tortuosity and the dynamic evolution of fracture geometry during reactive transport. Finally, transport is modeled under the assumption of complete mixing at pore junctions, which enhances effective dispersion. Reduced mixing would likely suppress lateral spreading and branching of reactive features and promote stronger localization near the fracture-matrix interface. Nevertheless, we expect the central mechanisms identified here–the competition between preferential fracture flow, lateral matrix infiltration, and precipitation-induced flow redistribution–to remain robust across a broad range of reactive fractured porous systems.

CRediT authorship contribution statement

Agnieszka Budek: Writing – original draft, Visualization, Software, Methodology, Investigation, Formal analysis; **Piotr Szymczak:** Writing – review & editing, Supervision, Methodology, Investigation, Conceptualization; **Peter K. Kang:** Writing – review & editing, Supervision, Investigation, Funding acquisition, Conceptualization.

Data availability

Data will be made available on request.

Declaration of competing interest

The authors declare that they have no known competing financial interests or personal relationships that could have appeared to influence the work reported in this paper.

Acknowledgment

Research supported as part of the Center on Geo-process in Mineral Carbon Storage, an Energy Frontier Research Center funded by the U.S. Department of Energy, Office of Science, Basic Energy Sciences at the University of Minnesota under award #DE-SC0023429. PKK and AB acknowledge the STEAM Program (RS-2024-00461440) from the National Research Foundation of Korea. PS acknowledges the support of the National Science Centre (Poland) under research Grant 2022/47/B/ST3/03395.

Supplementary material

Supplementary material associated with this article can be found in the online version at 10.1016/j.epsl.2026.120163.

References

Amestoy, P.R., Duff, I.S., Koster, J., L'Excellent, J.Y., 2001. A fully asynchronous multifrontal solver using distributed dynamic scheduling. SIAM J. Matrix Anal. Appl. 23 (1), 15–41.

Amestoy, P.R., Guermouche, A., L'Excellent, J.-Y., Pralet, S., 2006. Hybrid scheduling for the parallel solution of linear systems. Parallel Comput. 32 (2), 136–156.

Andreani, M., Luquot, L., Gouze, P., Godard, M., Hoise, E., Gibert, B., 2009. Experimental study of carbon sequestration reactions controlled by the percolation of CO_2-rich brine through peridotites. Environ. Sci. Tech. 43 (4), 1226–1231.

Beinlich, A., John, T., Vrijmoed, J.C., Tominaga, M., Magna, T., Podladchikov, Y.Y., 2020. Instantaneous rock transformations in the deep crust driven by reactive fluid flow. Nat. Geosci. 13 (4), 307–311.

Békri, S., Thovert, J.-F., Adler, P.M., 1997. Dissolution and deposition in fractures. Eng. Geol. 48, 283–308.

Budek, A., Garstecki, P., Samborski, A., Szymczak, P., 2015. Thin-finger growth and droplet pinch-off in miscible and immiscible displacements in a periodic network of microfluidic channels. Phys. Fluids 27 (11), 112109.
Budek, A., Szymczak, P., 2012. Network models of dissolution of porous media. Phys. Rev. E 86, 056318.
Budek, A., Szymczak, P., 2025. Channeling, clogging and permeability oscillations: different macroscopic regimes in mineral replacement. J. Geophys. Res. Solid Earth 130 (6), e2024JB031081.
Budek, A., Szawełło, T., Voller, V., Szymczak, P., 2026. Retreat to advance: self-blocking enables efficient mineral replacement. Geotech. Lett. https://doi.org/10.1680/jgele.25.00094.
Cabeza, Y., Hidalgo, J.J., Carrera, J., 2020. Competition is the underlying mechanism controlling viscous fingering and wormhole growth. Geophys. Res. Lett. 47 (3), e2019GL084795.
Centrella, S., Beaudoin, N.E., Derluyn, H., Motte, G., Hoareau, G., Lanari, P., Piccoli, F., Pecheyran, C., Callot, J.P., 2021. Micro-scale chemical and physical patterns in an interface of hydrothermal dolomitization reveals the governing transport mechanisms in nature: case of the layens anticline, pyrenees, france. Sedimentology 68 (2), 834–854.
Chadam, D., Hoff, D., Merino, E., Ortoleva, P., Sen, A., 1986. Reactive infiltration instabilities. IMA J. Appl. Math. 36, 207–221.
Cohen, C., Ding, D., Quintard, M., Bazin, B., 2008. From pore scale to wellbore scale: impact of geometry on wormhole growth in carbonate acidization. Chem. Eng. Sci. 63, 3088–3099.
Couder, Y., Maurer, J., González-Cinca, R., Hernández-Machado, A., 2005. Side-branch growth in two-dimensional dendrites. I. Experiments. Phys. Rev. E 71 (3), 31602.
Deng, H., Fitts, J.P., Crandall, D., McIntyre, D., Peters, C.A., 2015. Alterations of fractures in carbonate rocks by CO2-acidified brines. Environ. Sci. Technol. 49 (16), 10226–10234.
Deng, J., Sharma, R.P., Szymczak, P., Kang, P.K., 2025. Anomalous transport in dissolving porous media: transitions between Fickian and non-Fickian regimes. Geophys. Res. Lett. 52 (15), e2025GL115940.
Dijk, P., Berkowitz, B., Yechieli, Y., 2002. Measurement and analysis of dissolution patterns in rock fractures. Water Resour. Res. 38, 1013.
Dong, S., You, D., Guo, Z., Guo, C., Chen, D., 2018. Intense silicification of Ordovician carbonates in the Tarim Basin: constraints from fluid inclusion Rb–Sr isotope dating and geochemistry of quartz. Terra Nova 30 (6), 406–413.
Dreybrodt, W., 1990. The role of dissolution kinetics in the development of karst aquifers in limestone: A model simulation of karst evolution. J. Geol. 98, 639–655.
Economides, M.J., Nolte, K.G., 2000. Reservoir Stimulation. John Wiley and Sons.
Eriksson, N., Destouni, G., 1997. Combined effects of dissolution kinetics, secondary mineral precipitation, and preferential flow on copper leaching from mining waste rock. Water Resour. Res. 33 (3), 471–483.
Ford, D.C., Williams, P., 2007. Karst Hydrogeology and Geomorphology. Wiley, Chichester, UK.
Fowler, A.C., Yang, X.-S., 2003. Dissolution/precipitation mechanisms for diagenesis in sedimentary basins. J. Geophys. Res. Solid Earth 108 (B10).
Fredd, C.N., Fogler, H.S., 1998. Influence of transport and reaction on wormhole formation in porous media. AIChE J. 44, 1933–1949.
Garcia-Rios, M., Luquot, L., Soler, J.M., Cama, J., 2015. Influence of the flow rate on dissolution and precipitation features during percolation of CO2-rich sulfate solutions through fractured limestone samples. Chem. Geol. 414, 95–108.
Guo, S., Chu, X., Hermann, J., Chen, Y., Li, Q., Wu, F., Liu, C., Sein, K., 2021. Multiple episodes of fluid infiltration along a single metasomatic channel in metacarbonates (Mogok metamorphic belt, Myanmar) and implications for CO2 release in orogenic belts. J. Geophys. Res. Solid Earth 126 (1), e2020JB020988.
Hoefner, M.L., Fogler, H.S., 1988. Pore evolution and channel formation during flow and reaction in porous media. AIChE J. 34, 45–54.
Hollis, C., Bastesen, E., Boyce, A., Corlett, H., Gawthorpe, R., Hirani, J., Rotevatn, A., Whitaker, F., 2017. Fault-controlled dolomitization in a rift basin. Geology 45 (3), 219–222.
Jones, T.A., Detwiler, R.L., 2016. Fracture sealing by mineral precipitation: the role of small-scale mineral heterogeneity. Geophys. Res. Lett. 43 (14), 7564–7571.
Kaufmann, G., Gabrovšek, F., Romanov, D., 2016. Dissolution and precipitation of fractures in soluble rock. Hydrol. Earth Syst. Sci. Discuss. 2016, 1–30. https://doi.org/10.5194/hess-2016-372
Koeshidayatullah, A., Al-Sinawi, N., Swart, P.K., Boyce, A., Redfern, J., Hollis, C., 2022. Coevolution of diagenetic fronts and fluid-fracture pathways. Sci. Rep. 12 (1), 9278.
Kondratiuk, P., Tredak, H., Ladd, A. J.C., Szymczak, P., 2015. Synchronization of dissolution and precipitation fronts during infiltration-driven replacement in porous rocks. Geophys. Res. Lett. 42 (7), 2244–2252.
Kondratiuk, P., Tredak, H., Upadhyay, V., Ladd, A. J.C., Szymczak, P., 2017. Instabilities and finger formation in replacement fronts driven by an oversaturated solution. J. Geophys. Res. Solid Earth 122, 5972–5991.
Korzhinskii, D.S., 1968. The theory of metasomatic zoning. Miner. Deposita 231, 222–231.
Lee, W., Chen, M.A., Bresciani, E., Toner, B.M., Kang, P.K., 2025. Effects of pore-scale three-dimensional flow and fluid inertia on mineral dissolution. Water Resour. Res. 61 (4), e2024WR038176.
Lichtner, P.C., 1988. The quasi-stationary state approximation to coupled mass transport and fluid-rock interaction in a porous media. Geochim. Cosmochim. Acta 52, 143–165.
Lund, K., Fogler, H.S., 1976. Acidization-V. The prediction of the movement of acid and permeability fronts in sandstone. Chem. Eng. Sci. 31, 381–392.
Madondo, J., Canet, C., Nunez-Useche, F., Gonzalez-Partida, E., 2021. Geology and geochemistry of jasperoids from the 'Montaña de Manganeso' district, San Luis Potosí, north-central Mexico. Revista Mexicana de Ciencias Geológicas 38 (3), 193–209.
Matter, J.M., Kelemen, P.B., 2009. Permanent storage of carbon dioxide in geological reservoirs by mineral carbonation. Nat. Geosci. 2 (12), 837.
Matter, J.M., Stute, M., Snæbjörnsdottir, S.Ó., Oelkers, E.H., Gislason, S.R., Aradottir, E.S., Sigfusson, B., Gunnarsson, I., Sigurdardottir, H., Gunnlaugsson, E., et al., 2016. Rapid carbon mineralization for permanent disposal of anthropogenic carbon dioxide emissions. Science 352 (6291), 1312–1314.
Menke, H.P., Bijeljic, B., Andrew, M.G., Blunt, M.J., 2015. Dynamic three-dimensional pore-scale imaging of reaction in a carbonate at reservoir conditions. Environ. Sci. Technol. 49 (7), 4407–4414.
Merino, E., Canals, A., 2011. Self-accelerating dolomite-for-calcite replacement: self-organized dynamics of burial dolomitization and associated mineralization. Am. J. Sci. 311, 572–607.
Molins, S., Soulaine, C., Prasianakis, N.I., Abbasi, A., Poncet, P., Ladd, A. J.C., Starchenko, V., Roman, S., Trebotich, D., Tchelepi, H.A., et al., 2021. Simulation of mineral dissolution at the pore scale with evolving fluid-solid interfaces: review of approaches and benchmark problem set. Comput. Geosci. 25 (4), 1285–1318.
Montes-Hernandez, G., Findling, N., Renard, F., 2016. Dissolution-precipitation reactions controlling fast formation of dolomite under hydrothermal conditions. Appl. Geochem. 73, 169–177.
Nisbet, H., Buscarnera, G., Carey, J.W., Chen, M.A., Detournay, E., Huang, H., Hyman, J.D., Kang, P.K., Kang, Q., Labuz, J.F., et al., 2024. Carbon mineralization in fractured mafic and ultramafic rocks: a review. Rev. Geophys. 62 (4), e2023RG000815.
Nisbet, H., Li, R., Purswani, P., Chen, M., Yang, W., Neil, C., Kang, Q., Mohanty, K., Kang, P.K., Viswanathan, H., 2025. Mechanistic understanding of carbon mineralization in fracture systems using microfluidics. Lab Chip 25 (16), 4024–4037.
Nitschke, F., 2018. Numerical and Experimental Characterization of Dissolution and Precipitation Processes in Deep Geothermal Reservoirs. Ph.D. thesis. Dissertation, Karlsruhe, Karlsruher Institut für Technologie (KIT), 2017.
Noiriel, C., Gouze, P., Madé, B., 2013. 3D analysis of geometry and flow changes in a limestone fracture during dissolution. J. Hydrol. 486, 211–223.
Noiriel, C., Steefel, C.I., Yang, L., Bernard, D., 2016. Effects of pore-scale precipitation on permeability and flow. Adv. Water Resour. 95, 125–137.
Nooraiepour, M., Masoudi, M., Shokri, N., Hellevang, H., 2021. Probabilistic nucleation and crystal growth in porous medium: new insights from calcium carbonate precipitation on primary and secondary substrates. ACS Omega 6 (42), 28072–28083.
Oelkers, E.H., Gislason, S.R., Matter, J., 2008. Mineral carbonation of CO_2. Elements 4 (5), 333–337.
Ortoleva, P., Chadam, J., Merino, E., Sen, A., 1987. Geochemical self-organization II: the reactive-infiltration instability. Am. J. Sci. 287, 1008–1040.
Palmer, A.N., 1991. Origin and morphology of limestone caves. Geol. Soc. Am. Bull. 103, 1–21.
Pandey, S.N., Chaudhuri, A., Rajaram, H., Kelkar, S., 2015. Fracture transmissivity evolution due to silica dissolution/precipitation during geothermal heat extraction. Geothermics 57, 111–126.
Pisani, L., Antonellini, M., Bezerra, F. H.R., Carbone, C., Auler, A.S., Audra, P., La Bruna, V., Bertotti, G., Balsamo, F., Pontes, C. C.C., De Waele, J., 2022. Silicification, flow pathways, and deep-seated hypogene dissolution controlled by structural and stratigraphic variability in a carbonate-siliciclastic sequence (Brazil). Mar. Pet. Geol. 139, 105611.
Poonoosamy, J., Klinkenberg, M., Deissmann, G., Brandt, F., Bosbach, D., Mäder, U., Kosakowski, G., 2020. Effects of solution supersaturation on barite precipitation in porous media and consequences on permeability: experiments and modelling. Geochim. Cosmochim. Acta 270, 43–60.
Putnis, A., 2021. Fluid-mineral interactions: controlling coupled mechanisms of reaction, mass transfer and deformation. J. Petrol. 62 (12), egab092.
Putnis, A., Austrheim, H., 2012. Mechanisms of metasomatism and metamorphism on the local mineral scale: the role of dissolution-reprecipitation during mineral re-equilibration. In: Metasomatism and the Chemical Transformation of Rock: The Role of Fluids in Terrestrial and Extraterrestrial Processes. Springer, pp. 141–170.
Putnis, C.V., Mezger, K., 2004. A mechanism of mineral replacement: isotope tracing in the model system KCl-KBr-H2O. Geochim. Cosmochim. Acta 68 (13), 2839–2848.
Rege, S.D., Fogler, H.S., 1989. Competition among flow, dissolution, and precipitation in porous media. AIChE J. 35 (7), 1177–1185.
Roded, R., Szymczak, P., Holtzman, R., 2021. Wormholing in anisotropic media: pore-scale effect on large-scale patterns. Geophys. Res. Lett. 48 (11), e2021GL093659.
Ruiz-Agudo, E., Putnis, C.V., Putnis, A., 2014. Coupled dissolution and precipitation at mineral–fluid interfaces. Chem. Geol. 383, 132–146.
Sanna, A., Uibu, M., Caramanna, G., Kuusik, R., Maroto-Valer, M.M., 2014. A review of mineral carbonation technologies to sequester CO_2. Chem. Soc. Rev. 43, 8049.
Shafabakhsh, P., Cordonnier, B., Pluymakers, A., Le Borgne, T., Mathiesen, J., Linga, G., Hu, Y., Kaestner, A., Renard, F., 2024. 4D neutron imaging of solute transport and fluid flow in sandstone before and after mineral precipitation. Water Resour. Res. 60 (3), e2023WR036293.
Shah, R.K., London, A.L., 1978. Laminar Flow Forced Convection in Ducts: A Source Book for Compact Heat Exchanger Analytical Data. Academic Press, New York. https://doi.org/10.1016/C2013-0-04123-9
Shen, T., Miller, Q. R.S., Lahiri, N., Terry, O., Owen, A.T., Kou, Z., Schaef, H.T., Kelly, S.A., 2025. Multiphase flow regime controls carbonate precipitation morphologies during CO2 injection in subsurface basalts. Environ. Sci. Technol. 59 (38), 20345–20356.
Simpson, M.P., Christie, A.B., 2019. Hydrothermal alteration mineralogical footprints for new zealand epithermal au-ag deposits. N. Z. J. Geol. Geophys. 62 (4), 483–512.
Singurindy, O., Berkowitz, B., 2003. Evolution of hydraulic conductivity by precipitation and dissolution in carbonate rock. Water Resour. Res. 39 (1), 1016.
Soucey, C., Sutton, C., Yang, W., Zahasky, C., Kang, P.K., 2025. Deciphering solute and reactive transport in triple porosity systems: etched rock core experiments and numerical modeling. Environ. Sci. Technol. 59 (29), 15364–15374.

Starchenko, V., Marra, C.J., Ladd, A. J.C., 2016. Three-dimensional simulations of fracture dissolution. J. Geophys. Res. Solid Earth 121 (9), 6421–6444.
Szymczak, P., Ladd, A.J.C., 2006. A network model of channel competition in fracture dissolution. Geophys. Res. Lett. 33, L05401.
Ulrich, M., Munoz, M., Guillot, S., Cathelineau, M., Picard, C., Quesnel, B., Boulvais, P., Couteau, C., 2014. Dissolution–precipitation processes governing the carbonation and silicification of the serpentinite sole of the New Caledonia ophiolite. Contrib. Mineral. Petrol. 167 (1), 952.
Wang, T., Hu, R., Yang, Z., Zhou, C.-X., Chen, Y.-F., Zhou, C.-B., 2022. Transitions of dissolution patterns in rough fractures. Water Resour. Res. 58 (1), e2021WR030456. https://doi.org/10.1029/2021WR030456
Wilkinson, J.J., Eyre, S.L., Boyce, A.J., 2005. Ore-forming processes in Irish-type carbonate-hosted Zn-Pb deposits: evidence from mineralogy, chemistry, and isotopic composition of sulfides at the Lisheen mine. Econ. Geol. 100 (1), 63–86.
Witherspoon, P.A., Wang, J.S.Y., Iwai, K., Gale, J.T., 1980. Validity of cubic law for fluid flow in a deformable rock fracture. Water Resour. Res. 16 (6), 1016–1024.
Yang, F., Guan, D., Starchenko, V., Yuan, K., Stack, A.G., Ling, B., 2024a. Effect of nucleation heterogeneity on mineral precipitation in confined environments. Geophys. Res. Lett. 51 (9), e2023GL107185.
Yang, W., Chen, M.A., Lee, S.H., Kang, P.K., 2024b. Fluid inertia controls mineral precipitation and clogging in pore to network-scale flows. Proc. Natl. Acad. Sci. 121 (28), e2401318121.
You, D., Han, J., Hu, W., Qian, Y., Chen, Q., Xi, B., Ma, H., 2018. Characteristics and formation mechanisms of silicified carbonate reservoirs in well SN4 of the Tarim Basin. Energy Explor. Exploit. 36 (4), 820–849.
Zhang, C., Dehoff, K., Hess, N., Oostrom, M., Wietsma, T.W., Valocchi, A.J., Fouke, B.W., Werth, C.J., 2010. Pore-scale study of transverse mixing induced CaCO3 precipitation and permeability reduction in a model subsurface sedimentary system. Environ. Sci. Technol. 44 (20), 7833–7838.
Zhou, C.-X., Hu, R., Li, H.-W., Yang, Z., Chen, Y.-F., 2022. Pore-scale visualization and quantification of dissolution in microfluidic rough channels. Water Resour. Res. 58 (11), e2022WR032255.